# Experimental validation of Enhanced Magnetic Resonance Imaging (EMRI) using Particle Image Velocimetry (PIV)

Giacomo Annio[1], Ryo Torii[*2], Andrea Ducci[2],
Vivek Muthurangu[3], Victor Tsang[4], and Gaetano
Burriesci[*2,5]

[1]Dept of Medical Physics and Biomedical
engineering, University College London, London,
UK
[2]Dept of Mechanical Engineering, University
College London, London, UK
[3]Centre for Cardiovascular Imaging and Physics,
University College London, London, UK
[4]Cardiothoracic Surgery Unit, Great Ormond
Street Hospital, London, UK
[5]Ri.MED Foundation, Palermo, Italy

**Abstract** Flow-sensitive four-dimensional Cardiovascular Magnetic Resonance Imaging (4D Flow CMR) has increasingly been utilised to characterise patients' blood flow, in association with patiens' state of health and disease, even though spatial and temporal resolutions still constitute a limit. Computational fluid dynamics (CFD) is a powerful tool that could expand these information and, if integrated with experimentally-obtained velocity fields, would enable to derive a large variety of the flow descriptors of interest. However, the accuracy of the flow parameters is highly influenced by the quality of the input data such as the anatomical model and boundary conditions typically derived from medical images including 4D Flow CMR. We previously proposed a novel approach in which 4D Flow CMR and CFD velocity fields are integrated to obtain an Enhanced 4D Flow CMR (EMRI), allowing to overcome the spatial-resolution limitation of 4D Flow CMR, and enable an accurate quantification of flow. In this paper, the proposed approach is validated in a U bend channel, an idealised model of the human aortic arch. The flow patterns were studied with 4D Flow CMR, CFD and EMRI, and compared with high resolution 2D PIV experiments obtained in pulsatile conditions. The main strengths and limitations of 4D Flow CMR and CFD were illustrated by exploiting the accuracy of PIV by comparing against PIV velocity fields.
EMRI flow patterns showed a better qualitative and quantitative agreement with PIV results than the other techniques. EMRI enables to overcome the experimental

Corresponding authors: `r.torii@ucl.ac.uk`, `g.burriesci@ucl.ac.uk`

Address(es) of author(s) should be given

limitations of MRI-based velocity measurements and the modelling simplifications of CFD, allowing an accurate prediction of complex flow patterns observed experimentally, while satisfying mass and momentum balance equations.

**keywords:** 4D Flow CMR, PIV, CFD, U-bend, Cardiovascular flow.

## 1 Introduction

It has been shown that heamodynamic parameters, such as wall shear stress, play a significant role in the blood vessel remodelling and the development of cardiovascular diseases [1]. Yet, in everyday clinical practice, most parameters used for the assessment of cardiovascular diseases are based on anatomical evaluations rather than on the effect of diseases on local haemodynamics [2]. As small anatomical changes in the vessel geometry can affect dramatically the blood flow, resulting in pathological conditions [3], integration of flow-related parameters in the assessment of diseases has the vast potential to enrich diagnostics.

In recent years, the development of 2D Phase contrast magnetic resonance imaging (PC MRI) [4] and 4D Flow CMR sequences [5,6] have made non-invasive blood flow measurements accessible to clinicians. These tools allow 2D and 3D illustration of blood flow in the vascular region of interest, allowing a quantitative full field estimate of the velocity distribution. 4D Flow CMR is widely used for the assessment of the cardiac function and to perform flow quantification in a broad range of conditions, such as aortic coarctation, aortic dissection, pulmonary arteries diseases, valvular disease [7]. However, the relatively poor spatial resolution, still constitutes a major limitation, because it restricts the application to large vessels, and the acquisition needs to be done through averaging over several cardiac cycle, thus resulting in underestimation of the peak velocities [6] . Another limitation of MRI is noise, mainly caused by gradient induced eddy currents [8] and magnetic field inhomogeneities [9], which can be reduced by applying correction methods but reduce the accuracy of the acquired data. Another important issue affecting the reliability of the velocity measured with 4D Flow CMR is the velocity encoding, $v_{ENC}$, a parameter that must be specified before performing flow sensitive MRI. This needs to be set higher than the maximum expected flow velocity, so as to avoid velocity aliasing, or phase wraps, occurring when blood velocity magnitudes exceed the $v_{ENC}$ value. However, setting the $v_{ENC}$ too high would also cause an issue, especially in capturing velocities much lower than the $v_{ENC}$ [5]. Besides these limitations, 4D Flow CMR remains the most effective and versatile in-vivo non-invasive imaging technique for cardiovascular applications.

In the last few decades, the great advances in computing power and numerical techniques, together with the accessibility of 3D anatomical geometries and flow information by the advancement of medical imaging techniques, have accelerated the adoption of computational modelling to the study of cardiovascular problems [10]. Computational fluid dynamics (CFD) has been used in a broad range of applications, such as risk-free device testing [11,12], characterisation of cardiovascular conditions and intervention planning [13–15], providing estimate of local haemodynamics with high spatial and temporal resolutions, and the determination of essential parameters such as the local shear stress.

However, CFD models require a number of assumptions regarding the modelling of the arterial wall compliance [16], the rheological properties of the fluid

[17], and the choice of the boundary conditions at the inlet and outlet regions [18]. These influence the reliability of the simulation results, raising a question whether numerical models can provide a better accuracy than clinical measurements [19].

In order to overcome the limitations of 4D Flow CMR and CFD, whilst exploiting their respective potential, we recently proposed a novel approach, the enhanced magnetic resonance imaging (EMRI) [20]. This integrates the two approaches by feeding the experimentally measured velocity field data into a CFD model, so as to enforce the physics of the phenomenon (i.e. mass and momentum conservations) to greatly increase the reliability and resolution of the measurement. In this work, we present a validation of this new technique, comparing a complex pulsatile flow patterns based on 4D Flow CMR experiment, a standard CFD analysis and EMRI, against the in-vitro measurement, with particle image velocimetry (PIV), as the gold standard.

PIV is an optical non-intrusive quantitative technique capable of capturing instantaneous complex flow structures with high spatial resolution, and is widely adopted as validation tool for both numerical [21, 22, 15] and MRI [23, 24] studies. Pekkan et al. [15] used PIV to assess the prediction capability of a CFD model by studying the total cavo-pulmonary connection in steady flow condition. In this study CFD and PIV showed a remarkable agreement, especially considering the complexity of the anatomical region studied. However, the CFD velocities resulted systematically lower (max 15%) with respect to the one measured by PIV. This discrepancy may be explained by the unpolished interior model surfaces that could have introduced a background noise effect. Kitajima et al. [24] studied the flow in a stereo-lithographic replica of an extra-cardiac total cavo-pulmonary connection using PIV and PC-MRI. Their results highlight the degree of similarities between PIV and PC MRI but it is limited to a steady state scenario. PIV was compared with 4D Flow MRI by Medero et al. [25] to assess the difference in the estimation of velocity flow field and WSS in a patient-specific model of aneurysm. This work showed that there is a good quantitative and qualitative agreement between the two modalities and that the measured differences decrease when averaging in time and space the PIV to match the 4D Flow CMR resolution.

A quantitative comparison of high resolution 4D Flow CMR, PIV and CFD was carried out by Van Ooji et al. [23] by assessing the flow of a real size patient specific phantom of an intra-cranial aneurysm. Also this study confirmed that good qualitative and quantitative agreement exists between PC MRI measurements, CFD simulations and PIV measurements of flow patterns, on steady and pulsatile conditions, reporting that the difference between CFD simulations and 4D Flow CMR measurements (RMSE = 4–5 %) was smaller than that between PIV and 4D Flow CMR measurements (10–12 %). However these findings need to be carefully interpreted taking into account that a different fluid was used in the PIV experiment and in the 4D Flow CMR measurement and a scaling of the results measured with PIV was then necessary, which may have introduced bias. Moreover in this study a 4D Flow CMR sequence with a resolution of 0.2 x 0.33 x 0.2 mm$^3$ was used; in clinical practice the resolution is at least 5 times lower, raising an issue on the fundamental question about the ability of the clinical used sequences to correctly measure flow features in a reasonable scan time.

Specifically, the aim of this work is to assess the reliability of EMRI and verify its potential to further the concept of measure informed computational modelling and apply it in a clinical scenario. This is achieved by comparing the the flow
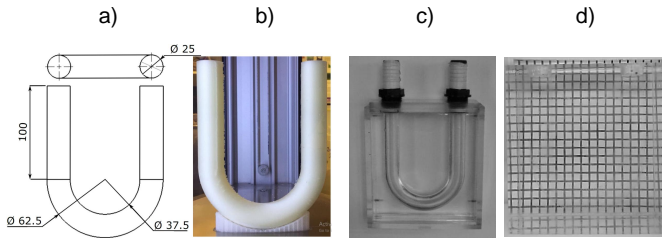
**Fig. 1** Geometry (a), PVA mold of the U bend pipe (b), U bend silicone phantom with (d) and without refractive index matched liquid (c).

patterns determined with this approach with those measured with a clinical 4D Flow CMR sequence, predicted by CFD and measured with PIV. Through the comparison, the advantages and limitations of each methods are highlighted.

## 2 Materials and Methods

### 2.1 Test rig

A U-bend pipe, providing an idealised and simplified representation of an aortic arch, was manufactured to be compatible with both PIV and MRI measurements (Figure 1 c). It was made by casting an optically clear, solvent free, low viscosity silicone elastomer (MED 6015, NuSil Technology, CA, USA) with a refractive index n = 1.4, using a perspex box and a soluble mould made from Polyvinyl Alcohol (PVA). The mould was designed with a CAD software (SolidWorks, Dassault Systems, Canada)(Figure 1 a) and then 3D printed in PVA using a Delta WASP 2040 Turbo 2 (Wasproject, Massa Lombarda, Italy) (Figure 1 b).

Following polymerisation of the silicone, the model was immersed in water, in order to dissolve the PVA mould and free the lumen of the U-bend pipe [26]. To minimise optical distortion, a liquid solution of the same refractive index as the silicone was prepared and used as working fluid. This consisted of a solution of water and glycerol (60 % by weight of the solution) resulting in a liquid with a density of 1150 kg · m$^{-3}$ and a viscosity of 0.008 Pa · s. Nearly neutrally buoyant hollow glass particles (Dantec Dynamics HGS-10, average nominal diameter $10^{-5}$ m) were dispersed in the fluid, to serve as seeding particles for the PIV analysis. A pulsatile flow was generated by means of a Pulsatile Blood Pump (Harvard Apparatus, UK), which was operated at 60 bpm, with a systole to diastole ratio of 40/60 and a stroke volume of 0.040 L.

The pump, the U bend and the working fluid reservoir were connected in series as shown in Figure 2.
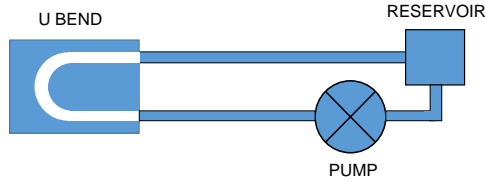
**Fig. 2** Diagram of the experimental rig.

2.2 PIV Experimental setup

A 2D PIV measurement system (TSI Inc., Minnesota, USA) was used to perform measurements of the velocity field in a plane by means of 2D phase resolved PIV. This techniques quantifies the fluid velocity distribution in a plane illuminated by a laser sheet (0.4 mm thick), by cross correlating the displacement of the visible seeding particles in the fluid, over a time interval $\Delta t$, calculated according to the the one-quarter rule [27]. Images were captured by a frame-straddling CCD camera (with a resolution of $2048 \times 2048$ pixels, TSI PowerViewTM Plus 4MP, TSI Inc., Minnesota) with a 52 mm lens (Nikon, Japan) placed orthogonally to the plane illuminated by the laser (Figure 4 a). A spatial resolution of $0.3717 \times 10^{-3}$ m was achieved by subdividing the U bend in 9 different regions of interest (Figure 3), which were analysed separately, merging together the results during the post processing phase.

According to the point of the cycle considered, the $\Delta t$ was varied in the range 300 - $500 \times 10^{-6}$ s ((1): $500 \times 10^{-6}$ s, (2): $300 \times 10^{-6}$ s, (3): $300 \times 10^{-6}$ s and (4): $500 \times 10^{-6}$ s).

Each PIV phase-locked experimental result was obtained by averaging the instantaneous velocity field of 100 different cycles (100 image pairs) for each of the four selected time points and for each of the 9 sections considered. Three instants were selected during systole and one in diastole, as shown in Figure 4 b and correspond to a time delay of $57 \times 10^{-3}$ s (1), $145 \times 10^{-3}$ s (2), $233 \times 10^{-3}$ s (3) and $527 \times 10^{-3}$ s (4) from the beginning of the systole. The post processing of the velocity maps was performed through Insight 4G$^{\text{TM}}$ (TSI Inc., US) and Matlab (The Mathworks, Natick, MA, USA).

The accuracy of the velocity profile was assessed by analysing the mass conservation [28]. Assuming axial symmetry of the velocity profile (which in this case is a reasonable approximation, as the captured images are in the middle plane of a cylindrical tube), and constant viscosity, the conservation of mass requires that the flow rate is consistent across the sections of the chosen ROI. Taking into consideration a region $A$ in the inlet segment of the U-bend, where $A$ is a $S \times P$ matrix, with $S$ the number of sections, and $P$ the number of pixels across the section ($s = 1, ..., S$, $p = 1, ..., P$) the average flow rate $FL_s$ at each instant is given by (Equation 1):
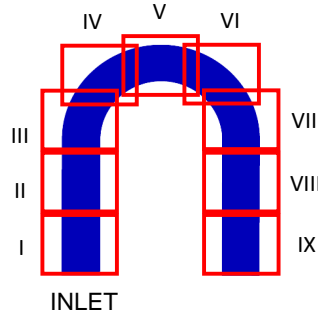
**Fig. 3** U bend with the 9 regions of interest imaged separately during the PIV experiment.

$$FL_s = \sum_{p}^{P} \pi x_p v_{s,p} d_{pix}, \tag{1}$$

where $x_i$ is the position along the diameter, $v_{s,i}(t)$ is the axial velocity at the $s$-th section and $i$-th pixel, and $d_{pix}$ is the pixel dimension. The minimum flow rate $FL_{min}$ and the maximum flow rate $FL_{max}$ were calculated to compute the percentage error $\epsilon_{PIV}$ using Equation 2:

$$\epsilon_{PIV} = \frac{FL_{Max} - FL_{min}}{FL_{max}} \tag{2}$$

The velocity maps obtained for each region of interest of the U-bend were merged together using Matlab (The Mathworks, Natick, MA, USA).

2.3 4D Flow CMR

The U-bend pipe was scanned with an ECG-gated 4D Flow CMR (Siemens) on a 1.5 T MRI scanner (Avanto MRI scanner, Siemens, Erlangen, Germany) at Great Ormond Street Hospital for Children (NHS Foundation Trust, London, UK). The MRI acquisition was triggered by the blood pump, and the parameters of the sequence used were TR $26.64 \times 10^{-3}$ s, TE $3.67 \times 10^{-3}$ s, flip angle $15^o$, matrix $160 \times 160$, pixel dimension $1.875 \times 1.875 \times 1.9$ mm$^3$, number of slices equal to 30, number of phases 32. Velocity encoding was made in three orthogonal directions: head-foot, right-left and anterior-posterior, with $v_{ENC}= 50$ cm $\cdot$ s$^{-1}$ equally in all 3 directions of acquisition. The image sets were acquired at 32 equally-spaced intervals over the pump cycle, corresponding to 192 volumetric image sets (32 time points $\times$ 3 encoding directions $\times$ pairs of magnitude and phase images), subsequently processed with an in-house Matlab code.

To assess the accuracy of the velocity field measured with the 4D Flow CMR, the standard deviation of the velocity was calculated using Equation 3 [29]:

$$\sigma_v = \frac{\sqrt{2} \cdot v_{ENC}}{\pi SNR}, \tag{3}$$

where $SNR$ is the signal-to-noise ratio of the magnitude images, calculated as the ratio of the average pixel intensity in two equally sized regions of interest, one in the U bend lumen (experiencing phase change) and the other in a stationary region. The standard deviation was assessed at the inlet, and in the three regions where the velocity profiles comparison were performed (Figure 5 b). To assess the quality of the velocity mapping, also the velocity-to-noise ratio $VNR$ was calculated as 4 [29]:

$$VNR = \frac{v}{\sigma_v},\qquad(4)$$

where $v$ is the measured velocity. As the $v_{ENC}$ value is set to exceed the peak velocity, this value is usually very high compared to velocity in diastole, which leads to a decrease of the $VNR$.

2.4 CFD Analysis

The CAD geometry of the phantom was meshed using ICEM CFD (ANSYS Inc, Cannonsburg, PA, USA) using tetrahedral elements and 10 layers of prism elements for the boundary layer near the wall. After running a grid independence test, the optimal mesh configuration was found to have 727498 nodes and 1697646 elements.

A time resolved CFD analysis was carried out over three cardiac cycles (with a time step of $1 \times 10^-3$ s). A fully developed parabolic velocity profile was imposed at the inlet, consistent with the measured flow waveform computed from the MRI data (shown in red in Figure 4 b, together with the velocity measured with PIV, blue points). At the exit of the tube, an outlet boundary condition with 0 Pa pressure was applied. The flow was assumed to be laminar and incompressible. The working fluid was modelled as Newtonian fluid, with density and viscosity equal to 1150 kg $\cdot$ m$^{-3}$ and 0.008 Pa $\cdot$ s, respectively. Walls were assumed to be rigid and a no-slip boundary condition was applied.

The simulations were conducted using the commercial computational fluid dynamic solver ANSYS CFX (version 18.0, ANSYS Inc. Cannonsburg PA, USA) using a standard desktop workstations (Intel Core i7 6700K 4GHz, 16GB RAM, 8 cores).

2.5 EMRI

EMRI algorithm [20] builds on the concept of measurement-informed computational modelling [30–32], where 4D Flow CMR data are provided to the CFD code to determine the flow which satisfies the governing equations and deviate the least from the measured data. The governing equations are the incompressible 3D Navier-Stokes equations, including the body force term as follows (5):

$$\rho\left(\frac{\partial \overline{v}}{\partial t} + \overline{v} \cdot \nabla \overline{v}\right) = -\nabla p + \mu\left(\nabla^2 \overline{v}\right) + \overline{f},\qquad(5)$$

$$\nabla \cdot \overline{v} = 0,\qquad(6)$$

where $\overline{v}$, $p$, $\rho$ and $\mu$ are the velocity, the pressure, the density and the viscosity of the fluid, respectively. The body force $\overline{f}$ is expressed as:

$$\overline{f} = K \cdot (\overline{v_{MRI}} - \overline{v_{CFD}}), \tag{7}$$

where the constant of proportionality $K$ is determined according to Equation 8:

$$K = k\frac{\rho U}{L}, \tag{8}$$

where $k$ is a constant, and $U$ and $L$ are the characteristic velocity and length scale of the system in this study. The body force $\overline{f}$ is updated at every convergence iteration within one time step, allowing the velocity field computed ($\overline{v_{CFD}}$) to converge towards the experimentally-acquired velocity field ($\overline{v_{MRI}}$). In this work, $k$ was kept constant, equal to 1, across the computational domain and over the entire simulation. The diameter and mean velocity at the inlet were chosen as U and L, respectively. Steady state EMRI simulations were conducted at the four time points selected for the PIV. Whilst the velocity correction towards the experimental velocity field is achieved through the body force term, EMRI algorithm still requires boundary conditions. A mass flow condition based on the volumetric flow rate from MRI measurement (Figure 4 b) at each time point of interest was applied at the inlet, without specifying any velocity profile. Zero pressure and no-slip conditions were applied at the outlet and at the wall boundaries, respectively. Other computational conditions, including the software and hardware computing platforms, were the same as those of the CFD analysis described in Section 2.4. The 4D Flow CMR data were first processed using an in-house code written in Matlab environment. Cartesian velocity fields were applied to the numerical model previously created for the CFD analysis, running the simulations using the same computational setup.

## 3 Results

The velocity maps of the longitudinal plane of the U bend (Figure 4 a) estimated with EMRI were compared with those derived from MRI and CFD, and validated against 2D PIV, in the selected instants of the cycle (Figure 4 b, time instants shown as the data points of PIV measurement)).

Furthermore, the 4D Flow CMR, CFD, EMRI and PIV velocity profiles were compared in three cross sections on the mid plane of U bend for each of the 4 instants considered (Figure 4 b). In order to assess the accuracy of the 4D Flow CMR measurements, CFD and EMRI computed velocities, the relative difference $\Delta$ with PIV measured velocity was computed at each pixel of the selected sections at the four time instants, using the following equation:

$$\Delta_p = \frac{\left| v_p^{PIV} - v_p^{C} \right|}{\left| v_{max}^{PIV} \right|}. \tag{9}$$

The relative percentage difference of each section was also computed as follows:

$$\Delta = \sum_{p}^{P} \frac{1}{P} \frac{\left| v_p^{PIV} - v_p^C \right|}{\left| v_{max}^{PIV} \right|}, \tag{10}$$

where $p = 1, ..., P$, with $P$ as the number of pixels across the section, and $v_p^{PIV}$ and $v_p^C$ are the velocity at the $p-th$ pixel measured with $PIV$ and acquired with CFD, EMRI or 4D Flow CMR, respectively. $v_{max}^{PIV}$ is the maximum velocity measured with PIV at each cross section and time instant. The flow regime is characterized by a Womersley number ($\alpha$) of 12.23, a peak Reynolds number $Re_{peak}$ of 977.8 and a temporally mean Reynolds number $Re_{mean}$ of 456.3. In unsteady conditions, the critical Reynolds number for the onset of turbulence decreases with the increase of the Womersley number, and the ratio $Re/\alpha = 200$ could be used as a threshold [33]. In this study, this ratio at the peak velocity is 89, less than a half of the threshold, therefore the flow should be considered in the laminar regime.

Another parameter used to assess the onset of turbulence is the critical Reynolds number $Re_{crit}$ as described by Peacock et al. [34]. This is computed as:

$$Re_{crit} = 169\alpha^{0.83} St^{-0.27}, \tag{11}$$

where $St$ is Strouhal number, calculated as:

$$St = \frac{Df}{2(v_{peak} - v_{mean})}, \tag{12}$$

with $D$ being the characteristic length of the system (in this case the diameter), $f$ is the pump cycle frequency, and $v_{peak}$ and $v_{mean}$ the peak and the mean velocity magnitude of the cycle, respectively. In the studied system, the $Re_{crit}$=2576.6, supporting that the system regime is expected to be laminar.

3.1 Velocity uncertainties

In Table 1, the percentage error $\epsilon_{piv}$ (Equation 2, computed using $S = 30$) is shown for each instant of the pump cycle selected for the PIV experiment. The $SNR$, the $VNR$ and the $\sigma_v$ of the 4D Flow CMR in the instant of the pump cycle considered for the comparison, are also presented. A higher uncertainty is observed, in terms of the percentage error of PIV measurement, at the first time instant.

**Table 1** $\Delta t$ (the laser delay), $\epsilon_{piv}$ of the PIV measurements and $SNR$, $VNR$ and $\sigma_v$ of the 4D Flow CMR data, at the different instants of the pump cycle, shown in Figure 4 b.

| Instant | $\Delta t$ $(\mu s)$ | $\epsilon_{PIV}$ (%) | SNR | VNR | $\sigma_v$ $(ms^{-1})$ |
|---|---|---|---|---|---|
| 1 | 500 | 11.41 | 12.04 | 4.07 | 0.0415 |
| 2 | 300 | 4.11 | 16.46 | 5.64 | 0.0443 |
| 3 | 300 | 4.28 | 15.71 | 8.3 | 0.0318 |
| 4 | 500 | 6.73 | 5.91 | 0.376 | 0.0845 |

3.2 Velocity maps

The average velocity at the inlet of the U-bend pipe during the pump cycle, measured with 4D Flow CMR and PIV (with the standard deviation), is plotted in Figure 4 b.

The average cross sectional velocities show a good agreement between the two sets of experimental data during systole, while some discrepancies are observed in diastole, with 4D Flow CMR velocities smaller than the PIV measurements. This is likely to be because, in this phase of the pump cycle, the velocity magnitude is much lower than the $v_{ENC}$ (5-fold smaller) and as a consequence the velocity encoded with MRI is less accurate. This is shown by the trend of the $v \pm \sigma_v$ (dashed lines in Figure 4 b).

Figure 4 c shows the velocity magnitude maps in the mid-plane (Figure 4 a) at the 4 selected instants, measured with 4D Flow CMR and PIV, and computed with CFD and EMRI.

Overall, there is a good qualitative agreement of the velocity distribution between all the different modalities.

The first time instant is during systolic acceleration. Considering PIV as the gold standard, the velocity magnitude in the outlet section and in the inner part of the arch is lower in the 4D Flow CMR measurement results. On the other hand, CFD shows much higher velocities in the whole domain. EMRI velocity is the closest one to the PIV result, in terms of magnitude and distribution.

A similar agreement can be identified when comparing the data from different modalities at time instant 2. Although the 4D Flow CMR velocity map shows good similarity to the PIV result, the outlet segment and the arch are characterised by lower velocities. CFD and EMRI show very good agreement with PIV in terms of velocity magnitude, although the flow patterns are better captured by EMRI, that corrects for the lower velocity that characterises MRI in the low velocities areas while preserving the flow structures.

In the third instant selected (instant 3), the velocity distribution is consistent across all the approaches, experimental, computational and hybrid. However, PIV shows less flow separation in the arch in comparison to the other techniques.

The last instant analysed is in the diastolic phase of the pump cycle (instant 4). The flow patterns obtained from the different approaches are in agreement. Nonetheless the CFD analysis presents higher velocity in the inlet segment, while the MRI shows lower velocity in the arch.

3.3 Velocity profiles

In order to have a quantitative comparison between the different approaches, the velocity profiles in three sections of the mid-plane (top row of Figure 5) at 4 instants of time, are compared (Figure 5).

Overall, 4D Flow CMR results show lower velocities in comparison to PIV (adopted as the gold standard), as also remarked during the analysis of the velocity maps. This is clearly evident in section B and C at instants 1 and 2.

On the other hand, the CFD analysis leads overall to slightly higher velocities compared to PIV. Moreover, velocity profiles predicted by CFD are different from those obtained with the other modalities, in almost all the sections analysed. The
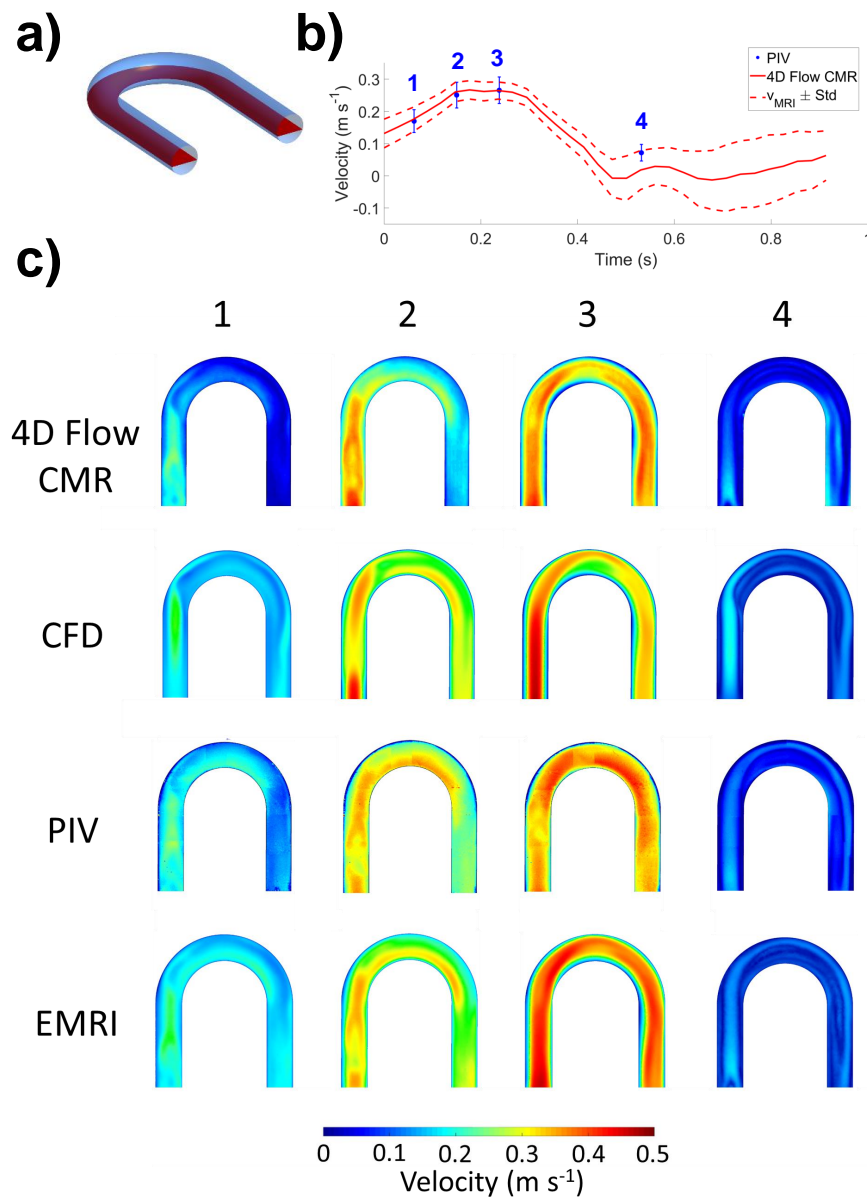
**Fig. 4** a) Plane selected for the comparison b) Average velocity at the inlet of the U bend during the pump cycle measured with 4D Flow CMR and PIV (with standard deviation, at the 4 instants of the cycle considered for the comparison) c) velocity maps in the selected plane at the 4 instant measured with 4D Flow CMR and PIV and computed with CFD and EMRI.
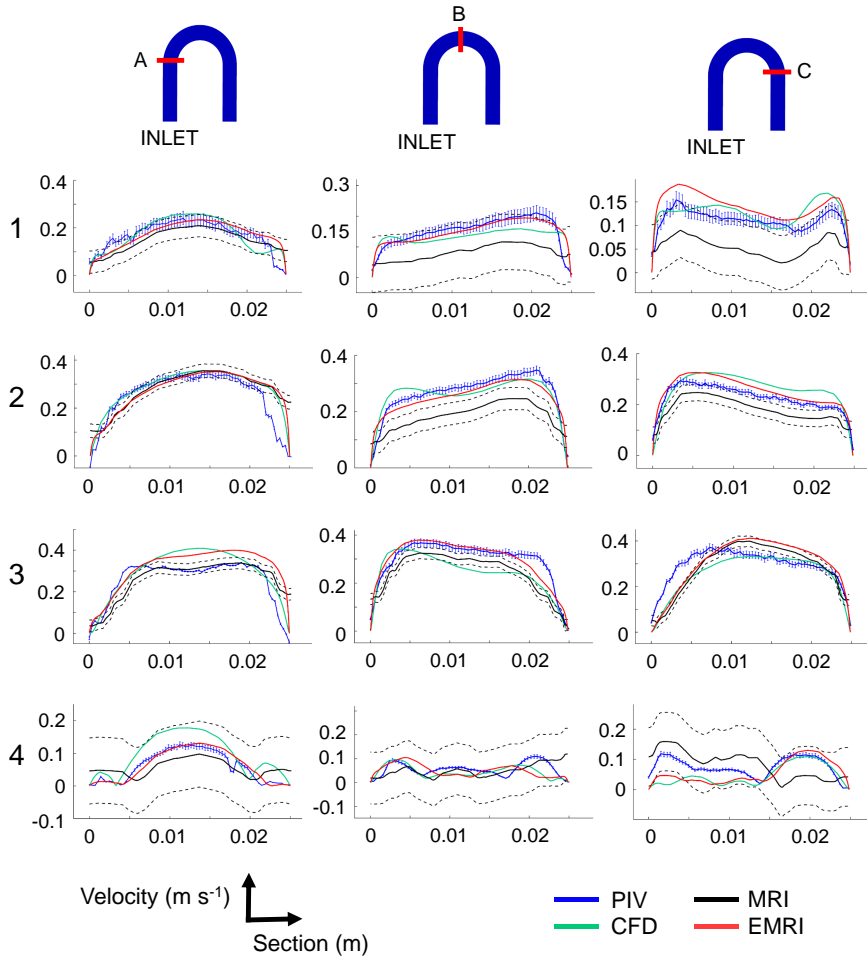
**Fig. 5** Velocity profiles in three sections of the U bend (indicated at the top of the figure) at the 4 instants of time considered, measured with 4D Flow CMR and PIV (with standard deviation) and computed with CFD and EMRI.

most typical example is Section B at time instant 2, where an additional peak near inside wall (distance $\approx 0.003$ m) of the curvature is observed in CFD velocity profile whilst the peak is not present in all other velocity profiles.

In general, EMRI velocity profiles are the closest to the ones measured with PIV. The EMRI velocity profiles show remarkable consistency with the PIV ones in particular at instants 1, 2 and 4 in section A, at instants 1, 2 and 4 in section B, and 2 and 3 in section C.

Using Equation 9, the relative difference between the velocity measured with PIV and the one computed with CFD/EMRI or measured with 4D Flow CMRI were computed in all the sections selected at the four time instants (Figure 6 - 8). In most of the cases, the highest differences between the velocity computed and measured are in the region in proximity of the wall, although it needs to be
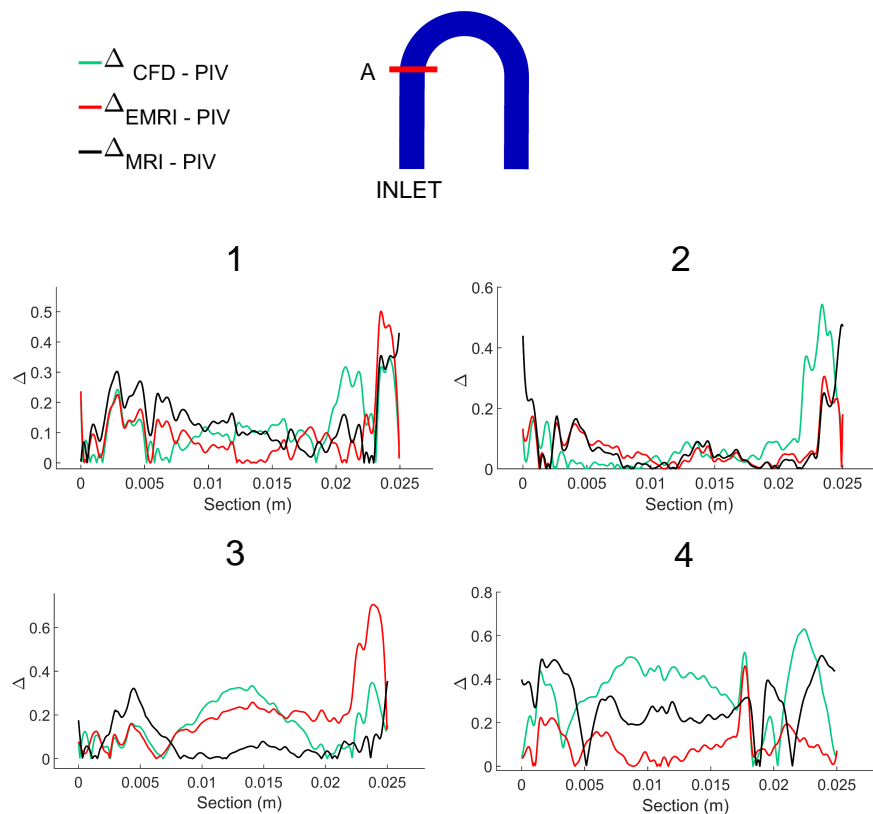
**Fig. 6** Relative difference between PIV and CFD, and PIV and EMRI velocity magnitudes ($v$) in section A at the 4 instant of time considered.

considered that PIV suffers from errors in the velocity estimation in these areas [35]. While CFD and EMRI show relative differences within the same range in all the sections, 4D Flow CMR relative difference is higher in sections B and C.

In Table 2, the relative difference of the velocity magnitude is computed at all the time instants in the different sections, comparing CFD, EMRI and MRI with PIV.

In section A, the agreement between EMRI and PIV is better in comparison to CFD at all the instants, except the third one. In this case, the EMRI overestimates the velocity as clear from Figure 5. In this section, the 4D Flow CMR agrees better with the reference flow in the systole, while in diastole the relative difference is higher.

Also in section B, the EMRI has a lower relative difference compared with CFD and 4D Flow CMR for all time instants but the forth one, where the $\Delta$ is
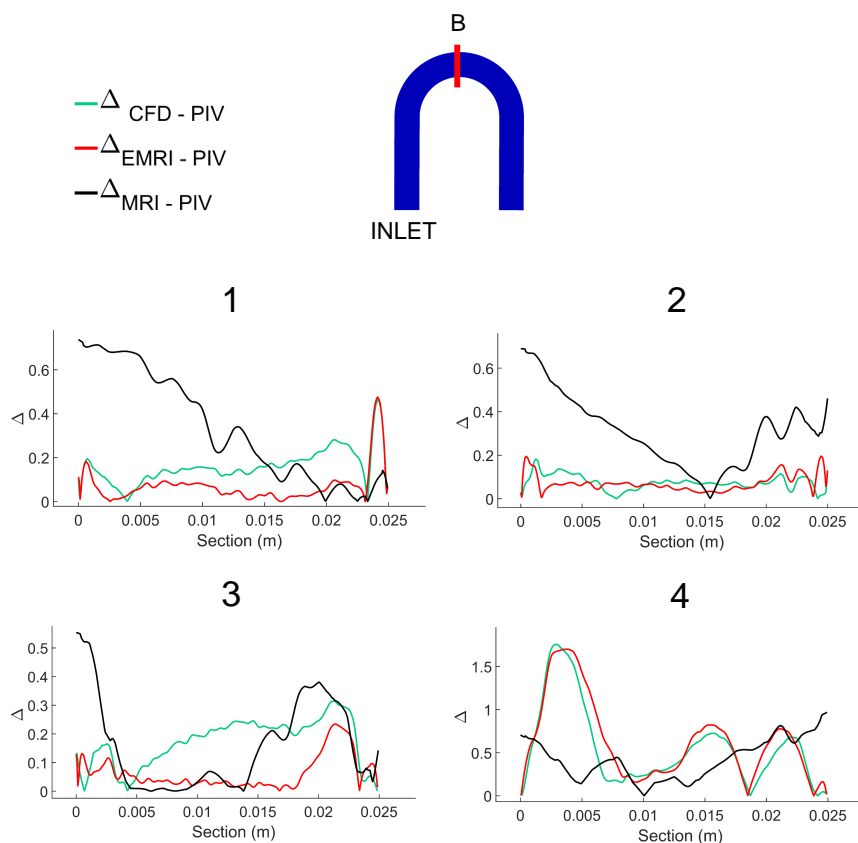
**Fig. 7** Relative difference between PIV and CFD, and PIV and EMRI velocity magnitudes ($v$) in section B at the 4 instant of time considered.

an order of magnitude higher with respect to the other instant and is higher than the one of MRI.

In section C, the relative difference of CFD and PIV is lower than the one between EMRI and PIV for all instants, except the second one. Therefore the CFD performs better compared to the EMRI, even though the relative differences are overall comparable.

Table 3 shows the $\Delta$ averaged over the sections at the time instants selected. Overall, EMRI computed velocities show higher agreement with the PIV results compared to CFD and 4D Flow CMR, especially in the systolic phase, when velocities are higher. In diastole, the relative difference is doubled. The CFD relative difference shows the same trend of EMRI, while the 4D Flow CMR relative difference is much larger in the accelerating phase of the systole and in diastole.
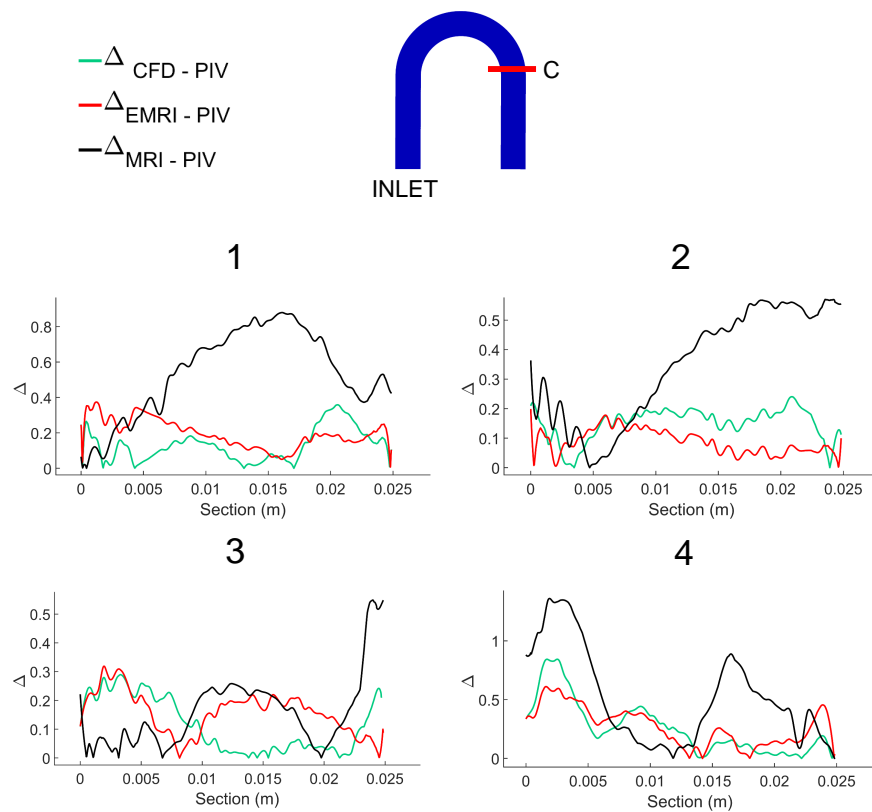
**Fig. 8** Relative difference between PIV and CFD, and PIV and EMRI velocity magnitudes ($v$) in section C at the 4 instant of time considered.

## 4 Discussion

This validation study identifies the main limitations of 4D Flow CMR and CFD. In particular, it is evident that the sensitivity of the MRI sequence to low velocities is highly compromised by the chosen $v_{ENC}$. This results in deviations of the velocity profiles between 4D Flow CMR and PIV, with an effect which is more pronounced during diastole, when the velocity becomes significantly lower than the selected velocity encoding.

In the MRI sequence used, the temporal resolution was selected such that cardiac cycle was covered by 32 time frames. This means that the velocities of each time point of the cycle was averaged over each time frame, increasing the $SNR$ [36]. However, the averaging of the signal over these time intervals, also leads to the underestimation of peak velocities, as observed in systole [37].

**Table 2** $\Delta_{PIV-CFD}$, $\Delta_{PIV-EMRI}$ and $\Delta_{MRI-PIV}$ for each section at the different instants of the pump cycle considered.

| Instants | Section A | Section B | Section C |
|---|---|---|---|
| | $\Delta_{PIV-CFD}$ | | |
| 1 | 0.1208 | 0.1590 | 0.1300 |
| 2 | 0.0873 | 0.0741 | 0.1508 |
| 3 | 0.1557 | 0.1720 | 0.1136 |
| 4 | 0.3457 | 0.5589 | 0.2569 |
| | $\Delta_{PIV-EMRI}$ | | |
| 1 | 0.0971 | 0.0704 | 0.1949 |
| 2 | 0.0652 | 0.0715 | 0.0875 |
| 3 | 0.1969 | 0.0634 | 0.1583 |
| 4 | 0.0981 | 0.6364 | 0.2713 |
| | $\Delta_{PIV-MRI}$ | | |
| 1 | 0.1367 | 0.3349 | 0.5410 |
| 2 | 0.0699 | 0.3082 | 0.3457 |
| 3 | 0.0728 | 0.1575 | 0.1565 |
| 4 | 0.2822 | 0.4212 | 0.5201 |

**Table 3** $\Delta$ for each time instant of the pump cycle considered, averaged over the sections considered.

| Instant | $\Delta_{PIV-CFD}$ | $\Delta_{PIV-EMRI}$ | $\Delta_{PIV-MRI}$ |
|---|---|---|---|
| 1 | 0.1366 | 0.1208 | 0.3375 |
| 2 | 0.1041 | 0.0748 | 0.2413 |
| 3 | 0.1471 | 0.1395 | 0.1289 |
| 4 | 0.3872 | 0.3353 | 0.4078 |

The lower velocity observed with 4D flow CMR could also be associated with the fact that the depth of the voxel is determined by the slice thickness. Usually, 4D flow CMR data is acquired in slices having a certain thickness different from the 'in-plane' resolution, thus the voxel is not isotropic. Here, the depth of a voxel, i.e. slice thickness, is larger than 'in-plane' pixel size. Being the slice thickness equal to 1.9 mm, the velocities measured in the plane of symmetry of the U-bend are averaged over this thickness, resulted in velocity underestimations as also reported by others [38].

Another main limitation of 4D Flow CMR is the partial volume effect that is predominant in the region close to the walls. Large variations of velocity is expected within a single voxel in these near-wall regions, which are averaged [39].

On the other hand, CFD appeared to overestimate velocities in the plane of symmetry and, similarly to MRI, was unable to match the experimental velocity profiles for all the instants and regions. These limitations are probably a consequence of the necessity to assume an idealised parabolic shaped velocity profile at the inlet. This approximation is common in computational studies for clinical applications [40, 41] and might lead to substantially different flow paths, that can have large impact on the assessment of cardiovascular diseases [18].

When EMRI is applied, the low sensitivity of 4D Flow CMR to low velocities is compensated by the need of satisfying the mass conservation, still leading to a realistic and fluid dynamically sound velocity distribution also in diastole.

Moreover, the non-slip condition and the presence of a high resolution mesh in the boundary layer allows the correction of the velocities in proximity of the wall, which in the 4D Flow CMR case are affected by large errors. This is a characteristic which is present in all the velocity profiles presented, and well reported in literature. This feature is of fundamental importance, especially when velocities in proximity of the wall are used for the calculation of flow derived parameters (e.g. WSS) in assessment of cardiovascular (patho)physiology [42,43].

Overall, the agreement between EMRI and PIV is significantly better than MRI and CFD alone. Some discrepancies between EMRI and PIV are however still observed in the velocity magnitude in section A at instant 3, section B and C at instants 3 and 4. This could be due to the inaccurate estimate of flow rate, used as the inflow condition of EMRI, quantified by means of 4D Flow CMR, in areas of low velocity, where the $SNR$ is low as the $v_{ENC}$ is substantially larger than the velocity of the fluid, and could lead to an incorrect estimation of the secondary velocity field. Multiple $v_{ENC}$ could have been adopted but the aim of the study is to use clinical 4D Flow CMR sequences which are usually single $v_{ENC}$.

Moreover, it should be considered that the velocity profiles acquired using PIV also involve experimental uncertainties. In particular, the PIV velocity maps of the U-bend were obtained as a composition of result from 9 different experiments. Although these experiments were conducted all in one session, to limit the change in the experimental conditions, the camera and the laser had to be moved to image each of the U-bend pipe portions. Furthermore after the post processing of each section, the velocity maps had to be registered to the U-bend geometry, to obtain the full U-bend velocity map.

PIV measurements were carried out on planes parallel to the tube axis because the dominant velocity component of the flow was intended to be used for the validation of EMRI. Moreover the out of plane velocity field is highly heterogeneous, impeding the use of one delay only between the two laser pulses and making therefore the acquisition of the out-of-plane velocity component unreliable for validation purposes.

Another limitation of this study concerns the use of PIV as a gold standard for velocities even in the areas close to the walls. In fact, similarly to 4D Flow CMR, the edges of PIV measurement windows are characterised by higher standard deviation values in comparison to bulk flow, presenting non-zero velocity on the wall. This is clearly shown also in the relative velocity difference profiles. A common cause of this problem is non-uniform particles distribution in proximity of the wall and the Gaussian low-pass filter applied during the processing, which helps the recognition of the particle in the subsequent processing steps, but biases the locations of the correlation peak in the case of near-wall flow investigations [35]. Nonetheless, these regions of higher uncertainty are spatially far smaller for PIV than for 4D Flow CMR, thus, in this study, we considered PIV as the gold standard in all spatial areas.

## 5 Conclusions

In this paper, EMRI (Enhanced Magnetic Resonance Imaging), a method integrating 4D Flow CMR and CFD, is validated on a pulsatile flow through a U-bend pipe. In particular, the ability of EMRI to replicate experimental measurements obtained by Particle Image Velocimetry were compared with the 4D Flow CMR measurements and standard CFD predictions. EMRI flow patterns showed a better qualitative and quantitative agreement with PIV results than the other techniques. In fact, the approach allows the correction of the measurement errors in MRI by enforcing the correct physics, achieving high resolution. Hence, EMRI enables to overcome the experimental limitations of MRI-based velocity measurements and the modelling simplifications of CFD, allowing a more accurate prediction of complex flow patterns observed experimentally, while maintaining fluid mechanically sound representation of the flow field. Further works still need to be conducted to assess the accuracy of the EMRI estimate of the velocity field in proximity of the wall. This would benefit haemodynamic computations by providing a way to estimate flow derived parameter such as wall shear stress.

This methodology, which can still be improved by including dynamical solutions, could play a major role in the clinical environment, giving access to fluid dynamic quantities directly linked with cardiovascular diseases such as atherosclerosis [44] and aneurysms [45]. Hence, the methods demonstrates the potential to establish as a useful diagnostic tool for the clinical analysis of cardiovascular diseases.

## Conflict of Interest

Conflict of interest statement.

## References

1. Adel M. Malek, Seth L. Alper, and Seigo Izumo. Hemodynamic shear stress and its role in atherosclerosis. *Journal of the American Medical Association*, 282(21):2035–2042, 1999.
2. C. Canstein, P. Cachot, A. Faust, A. F. Stalder, J. Bock, A. Frydrychowicz, J. Küffer, J. Hennig, and Michael Markl. 3D MR flow analysis in realistic rapid-prototyping model systems of the thoracic aorta: Comparison with in vivo data and computational fluid dynamics in identical vessel geometries. *Magnetic Resonance in Medicine*, 59(3):535–546, 2008.
3. Alex Frydrychowicz, Ernst Weigang, Andreas Harloff, Friedhelm Beyersdorf, Jürgen Hennig, Mathias Langer, and Michael Markl. Time-resolved 3-dimensional magnetic resonance velocity mapping at 3 T reveals drastic changes in flow patterns in a partially thrombosed aortic arch. *Circulation*, 113(11):460–461, 2006.
4. DB and others Nayler, GL and Firmin, DN and Longmore. Blood flow imaging by cine magnetic resonance. *J Comput Assist Tomogr*, 10(5):715—-722, 1986.

5. Petter Dyverfeldt, Malenka Bissell, Alex J. Barker, Ann F. Bolger, Carl Johan Carlhäll, Tino Ebbers, Christopher J. Francios, Alex Frydrychowicz, Julia Geiger, Daniel Giese, Michael D. Hope, Philip J. Kilner, Sebastian Kozerke, Saul Myerson, Stefan Neubauer, Oliver Wieben, and Michael Markl. 4D flow cardiovascular magnetic resonance consensus statement. *Journal of Cardiovascular Magnetic Resonance*, 17(1):1–19, 2015.

6. Michael Markl, Frandics P. Chan, Marcus T. Alley, Kris L. Wedding, Mary T. Draney, Chris J. Elkins, David W. Parker, Ryan Wicker, Charles A. Taylor, Robert J. Herfkens, and Norbert J. Pelc. Time-resolved three-dimensional phase-contrast MRI. *Journal of Magnetic Resonance Imaging*, 17(4):499–506, 2003.

7. Monvadi B. Srichai, Ruth P. Lim, Samson Wong, and Vivian S. Lee. Cardiovascular applications of phase-contrast MRI. *American Journal of Roentgenology*, 192(3):662–675, 2009.

8. Gary H Bernstein, Mat A and Zhou, Xiaohong Joe and Polzin, Jason A and King, Kevin F and Ganin, Alexander and Pelc, Norbert J and Glover. Concomitant gradient terms in phase contrast MR: analysis and correction. *Magnetic resonance in medicine*, 39(2):300–308, 1998.

9. Johannes M. Peeters, Clemens Bos, and Chris J.G. Bakker. Analysis and correction of gradient nonlinearity and B0 inhomogeneity related scaling errors in two-dimensional phase contrast flow measurements. *Magnetic Resonance in Medicine*, 53(1):126–133, 2005.

10. Paul D. Morris, Andrew Narracott, Hendrik Von Tengg-Kobligk, Daniel Alejandro Silva Soto, Sarah Hsiao, Angela Lungu, Paul Evans, Neil W. Bressloff, Patricia V. Lawford, D. Rodney Hose, and Julian P. Gunn. Computational fluid dynamics modelling in cardiovascular medicine. *Heart*, 102(1):18–28, 2016.

11. Marco Laumen, Tim Kaufmann, Daniel Timms, Peter Schlanstein, Sebastian Jansen, Shaun Gregory, Kai Chun Wong, Thomas Schmitz-Rode, and Ulrich Steinseifer. Flow analysis of ventricular assist device inflow and outflow cannula positioning using a naturally shaped ventricle and aortic branch. *Artificial Organs*, 34(10):798–806, 2010.

12. Nicolas Foin, Ryo Torii, Peter Mortier, Mathieu De Beule, Nicola Viceconte, Pak Hei Chan, Justin E. Davies, Xiao Yun Xu, Rob Krams, and Carlo Di Mario. Kissing balloon or sequential dilation of the side branch and main vessel for provisional stenting of bifurcations: Lessons from micro-computed tomography and computational simulations. *JACC: Cardiovascular Interventions*, 5(1):47–56, 2012.

13. Kwong Ming Tse, Peixuan Chiu, Heow Pueh Lee, and Pei Ho. Investigation of hemodynamics in the development of dissecting aneurysm within patient-specific dissecting aneurismal aortas using computational fluid dynamics (CFD) simulations. *Journal of Biomechanics*, 44(5):827–836, 2011.

14. Mirko Bonfanti, Stavroula Balabani, John P. Greenwood, Sapna Puppala, Shervanthi Homer-Vanniasinkam, and Vanessa Diáz-Zuccarini. Computational tools for clinical support: A multi-scale compliant model for haemodynamic simulations in an aortic dissection based on multi-modal imaging data. *Journal of the Royal Society Interface*, 14(136), 2017.

15. Kerem Pekkan, Diane De Zélicourt, Liang Ge, Fotis Sotiropoulos, David Frakes, Mark A. Fogel, and Ajit P. Yoganathan. Physics-driven CFD modeling of complex anatomical cardiovascular flows - A TCPC case study. *Annals of Biomedical Engineering*, 33(3):284–300, 2005.

16. Suo Jin, John Oshinski, and Don P. Giddens. Effects of wall motion and compliance on flow patterns in the ascending aorta. *Journal of Biomechanical Engineering*, 125(3):347–354, 2003.

17. Siobhan O'Callaghan, Michael Walsh, and Timothy McGloughlin. Numerical modelling of Newtonian and non-Newtonian representation of blood in a distal end-to-side vascular bypass graft anastomosis. *Medical Engineering and Physics*, 28(1 SPEC. ISS.):70–74, 2006.

18. Umberto Morbiducci, Raffaele Ponzini, Diego Gallo, Cristina Bignardi, and Giovanna Rizzo. Inflow boundary conditions for image-based computational hemodynamics: Impact of idealized versus measured velocity profiles in the human aorta. *Journal of Biomechanics*, 46(1):102–109, 2013.

19. David A. Steinman and Francesco Migliavacca. Editorial: Special Issue on Verification, Validation, and Uncertainty Quantification of Cardiovascular Models: Towards Effective VVUQ for Translating Cardiovascular Modelling to Clinical Utility. *Cardiovascular Engineering and Technology*, 9(4):539–543, 2018.

20. Giacomo Annio, Ryo Torii, Ben Ariff, Declan P. O'Regan, Vivek Muthurangu, Andrea Ducci, Victor Tsang, and Gaetano Burriesci. Enhancing Magnetic Resonance Imaging

With Computational Fluid Dynamics. *Journal of Engineering and Science in Medical Diagnostics and Therapy*, 2(4):1–11, 2019.

21. Anna Maria Tango, Jacob Salmonsmith, Andrea Ducci, and Gaetano Burriesci. Validation and Extension of a Fluid–Structure Interaction Model of the Healthy Aortic Valve. *Cardiovascular Engineering and Technology*, 9(4):739–751, 2018.

22. Matthew D. Ford, Hristo N. Nikolov, Jaques S. Milner, Stephen P. Lownie, Edwin M. De-Mont, Wojciech Kalata, Francis Loth, David W. Holdsworth, and David A. Steinman. PIV-measured versus CFD-predicted flow dynamics in anatomically realistic cerebral aneurysm models. *Journal of Biomechanical Engineering*, 130(2):1–9, 2008.

23. P. van Ooij, A. Guédon, C. Poelma, J. Schneiders, M. C M Rutten, H. A. Marquering, C. B. Majoie, E. van Bavel, and A. J. Nederveen. Complex flow patterns in a real-size intracranial aneurysm phantom: Phase contrast MRI compared with particle image velocimetry and computational fluid dynamics. *NMR in Biomedicine*, 25(1):14–26, 2012.

24. Hiroumi D. Kitajima, Kartik S. Sundareswaran, Thomas Z. Teisseyre, Garrett W. Astary, W. James Parks, Oskar Skrinjar, John N. Oshinski, and Ajit P. Yoganathan. Comparison of Particle Image Velocimetry and Phase Contrast MRI in a Patient-Specific Extracardiac Total Cavopulmonary Connection. *Journal of Biomechanical Engineering*, 130(4):041004, 2008.

25. Rafael Medero, Katrina Ruedinger, David Rutkowski, Kevin Johnson, and Alejandro Roldán-Alzate. In vitro assessment of flow variability in an intracranial aneurysm model using 4d flow mri and tomographic piv. *Annals of Biomedical Engineering*, 48(10):2484–2493, 2020.

26. Giacomo Annio, Gaia Franzetti, Mirko Bonfanti, Antonio Gallarello, Andrea Palombi, Elena De Momi, Shervanthi Homer-Vanniasinkam, Helge Wurdemann, Victor Tsang, Vanessa Diaz-Zuccarini, Ryo Torii, Stavroula Balabani, and Gaetano Burriesci. Low Cost Fabrication of PVA Based Personalized Vascular Phantoms for in Vitro Haemodynamic Studies: Three Applications. *Journal of Engineering and Science in Medical Diagnostics and Therapy*, 3(3):1–8, 2019.

27. Markus Raffel, Christian E Willert, Fulvio Scarano, Christian J Kähler, Steve T Wereley, and Jürgen Kompenhans. *Particle image velocimetry: a practical guide*. Springer, 2018.

28. Joseph M. Sherwood, David Holmes, Efstathios Kaliviotis, and Stavroula Balabani. Spatial distributions of red blood cells significantly alter local haemodynamics. *PLoS ONE*, 9(6), 2014.

29. Anders Nilsson, Karin Markenroth Bloch, Marcus Carlsson, Einar Heiberg, and Freddy Ståhlberg. Variable velocity encoding in a three-dimensional, three-directional phase contrast sequence: Evaluation in phantom and volunteers. *Journal of Magnetic Resonance Imaging*, 36(6):1450–1459, 2012.

30. T Hayase and S Hayashi. State Estimator of Flow as an Integrated Computational Method With Feedback of Online Experimental Measurement. *Journal of Fluids Engineering*, 119(December 1997):814–822, 1997.

31. Kenichi Funamoto, Yoshitsugu Suzuki, Toshiyuki Hayase, Takashi Kosugi, and Haruo Isoda. Numerical validation of MR-measurement-integrated simulation of blood flow in a cerebral aneurysm. *Annals of Biomedical Engineering*, 37(6):1105–1116, 2009.

32. Vinicius C. Rispoli, Jon F. Nielsen, Krishna S. Nayak, and Joao L. A. Carvalho. Computational fluid dynamics simulations of blood flow regularized by 3D phase contrast MRI. *BioMedical Engineering OnLine*, 14(1):110, 2015.

33. R. Trip, D. J. Kuik, J. Westerweel, and C. Poelma. An experimental study of transitional pulsatile pipe flow. *Physics of Fluids*, 24(1), 2012.

34. J. Peacock, T. Jones, C. Tock, and R. Lutz. The onset of turbulence in physiological pulsatile flow in a straight tube. *Experiments in Fluids*, 24(1):1–9, 1998.

35. Christian J. Kähler, Sven Scharnowski, and Christian Cierpka. On the uncertainty of digital PIV and PTV near walls. *Experiments in Fluids*, 52(6):1641–1656, 2012.

36. Timothy J Carr, James C and Carroll. *Magnetic resonance angiography: principles and applications*. Springer Science \& Business Media, 2011.

37. J. S. Milner, J. A. Moore, B. K. Rutt, and D. A. Steinman. Hemodynamics of human carotid artery bifurcations: Computational studies with models reconstructed from magnetic resonance imaging of normal subjects. *Journal of Vascular Surgery*, 28(1):143–156, 1998.

38. Ramkumar Krishnamurthy, Benjamin Cheong, and Raja Muthupillai. Tools for cardiovascular magnetic resonance imaging. *Cardiovascular diagnosis and therapy*, 4(2):104, 2014.

39. Loic Boussel, Vitaliy Rayz, Alastair Martin, Gabriel Acevedo-Bolton, Michael T. Lawton, Randall Higashida, Wade S. Smith, William L. Young, and David Saloner. Phase-contrast magnetic resonance imaging measurements in intracranial aneurysms in vivo of flow patterns, velocity fields, and wall shear stress: Comparison with computational fluid dynamics. *Magnetic Resonance in Medicine*, 61(2):409–417, 2009.
40. Liam Morris, Patrick Delassus, Pierce Grace, Fintin Wallis, Michael Walsh, and Tim Mc-Gloughlin. Effects of flat, parabolic and realistic steady flow inlet profiles on idealised and realistic stent graft fits through Abdominal Aortic Aneurysms (AAA). *Medical Engineering and Physics*, 28(1 SPEC. ISS.):19–26, 2006.
41. Senol Piskin and M. Serdar Celebi. Analysis of the effects of different pulsatile inlet profiles on the hemodynamical properties of blood flow in patient specific carotid artery with stenosis. *Computers in Biology and Medicine*, 43(6):717–728, 2013.
42. Michael Markl, Wolf Wallis, and Andreas Harloff. Reproducibility of flow and wall shear stress analysis using flow-sensitive four-dimensional MRI. *Journal of Magnetic Resonance Imaging*, 33(4):988–994, 2011.
43. Merih Cibis, Wouter V. Potters, Frank J.H. Gijsen, Henk Marquering, Ed VanBavel, Antonius F.W. van der Steen, Aart J. Nederveen, and Jolanda J. Wentzel. Wall shear stress calculations based on 3D cine phase contrast MRI and computational fluid dynamics: A comparison study in healthy carotid arteries. *NMR in Biomedicine*, 27(7):826–834, 2014.
44. Grégory Franck, Guillaume Even, Alexandre Gautier, Manuel Salinas, Alexia Loste, Emanuele Procopio, Anh Thu Gaston, Marion Morvan, Sébastien Dupont, Catherine Deschildre, Sophie Berissi, Jamila Laschet, Patrick Nataf, Antonino Nicoletti, Jean Baptiste Michel, and Giuseppina Caligiuri. Haemodynamic stress-induced breaches of the arterial intima trigger inflammation and drive atherogenesis. *European Heart Journal*, 40(11):928–937, 2019.
45. M. Shojima. Magnitude and Role of Wall Shear Stress on Cerebral Aneurysm. Computational Fluid Dynamic Study of 20 Middle Cerebral Artery Aneurysms. *Stroke*, 2004.